



ORIGINAL RESEARCH ARTICLE

The Effect of MB40 Addition on the Electrochemical Corrosion Resistance of an NdFeB Magnet Recycled from Electronic Waste

Mohamed Mehenni, Azzeddine Lounis, Fatma Ahnia, Djamel Miroud, Amar Manseri, and Mohamed Trari

Submitted: 22 June 2023 / Revised: 23 May 2024 / Accepted: 8 July 2024

A Ni-Cr alloy powder, designated MB40, with an average size of $30.5 \mu\text{m}$, was used as a grain boundary modifier in a recycled neodymium-iron-boron (Nd-Fe-B) matrix to improve the corrosion resistance, coercivity and other properties of the rare-earth sintered magnet. Nd-Fe-B powder with an average grain size of $95.1 \mu\text{m}$ was obtained by milling. The effects of doping with different amounts of MB40 (0, 0.5 and 1 wt.%) on the properties of the recycled magnet compared with an initial magnet were investigated. X-Ray Diffraction analysis revealed the formation of the $\text{Fe}_1\text{Nd}_1\text{Ni}_4$ and NiCrFe phases, after sintering, as well as the tetragonal phase $\text{Nd}_2\text{Fe}_{14}\text{B}$ matrix phase in the magnet doped with 1 wt.% of MB40. Scanning Electron Microscopy images coupled with energy-dispersive x-ray spectroscopy demonstrated that in the sample doped with 1 wt.% MB40, Cr-Ni diffuses into the grain boundaries, thus improving the microstructure of the magnet. Electrochemical Impedance Spectroscopy and potentiodynamic polarization were employed for corrosion characterization. The magnet doped with 1wt.% MB40 exhibited the highest corrosion potential ($E_{\text{corr}} = -696 \text{ mV}$), polarization resistance ($R_p = 1151.2 \Omega\text{-cm}^2$) and a low corrosion rate (V_{corr}) of $4.34 \mu\text{m}\cdot\text{year}^{-1}$ compared to the starting (initial) sample. The optimum characteristics of recycled NdFeB were obtained by blending milled NdFeB powder with 1 wt.% MB40, achieving the best values for product energy (BH_{max}), coercivity (H_c) and hardness, respectively 48.03 MGOe, 10.8 KOe and 587 HV.

Keywords corrosion resistance, doping powder, grain boundary modifier, NdFeB, rare earth magnets

1. Introduction

Recycling is an important and necessary practice for preserving natural resources and reducing electronic waste. Rare Earth Magnets (REM) like NdFeB (Neodymium-Iron-Boron) and SmCo (Samarium-Cobalt) (Ref 1, 2), are widely used in a variety of applications including hard drives, micro-robotics, biomedical engineering and electric vehicles among others (Ref 3, 4). They are made from a combination of Rare Earth Elements (REE), such as Nd, Pr, Dy, and Sm, which are limited resources and expensive to extract. Recycling therefore makes it possible to recover these precious metals to reuse them in the manufacture of new products. This considerably reduces their demand and limits the environmental impact linked to their extraction (Ref 5, 6). The growing use of $\text{Nd}_2\text{Fe}_{14}\text{B}$ magnets in a wide range of applications, including generators and electric motors, has led to a reassessment of their properties, such as corrosion resistance. (Ref 7). Ultimately, recycling $\text{Nd}_2\text{Fe}_{14}\text{B}$ magnets is an important step towards a sustainable and eco-friendly future with clean energy (Ref 8-12).

Zakotnik et al. (Ref 13) recycled $\text{Nd}_2\text{Fe}_{14}\text{B}$ magnet using electronic waste as raw material (VCM disk drives) while Weiqiang et al. (Ref 14) recycled NdFeB magnet by adding 1wt.% of DyH_3 . Additionally, Chuewangkam et al., improved functional properties of cement pastes by introducing hard magnetic NdFeB powders of into cement mixtures (Ref 15). Indeed, recycling Nd-Fe-B magnets seems a possible and interesting approach (Ref 16). However, despite their exceptional magnetic properties, NdFeB magnets are susceptible to corrosion, an undesirable process that alters the magnets'

Supplementary Information The online version contains supplementary material available at <https://doi.org/10.1007/s11665-024-10060-1>.

Mohamed Mehenni, Azzeddine Lounis, and Djamel Miroud, Laboratory of Sciences and Material Engineering (LSGM), Faculty of Mechanical and Process Engineering, University of Sciences and Technology, Houari Boumediene (USTHB), BP32 El Alia, Bab Ezzouar, 16111 Algiers, Algeria; **Fatma Ahnia**, Laboratory of Sciences and Material Engineering (LSGM), Faculty of Mechanical and Process Engineering, University of Sciences and Technology, Houari Boumediene (USTHB), BP32 El Alia, Bab Ezzouar, 16111 Algiers, Algeria; and Faculté de Technologie, Département de Génie Mécanique, Université de Bejaïa, 06000 Bejaïa, Algeria; **Amar Manseri**, Research Center on Semiconductors Technology for Energetics, CRTSE-TESE - 02, Bd. Dr. Frantz Fanon, 7 Merveilles, Box 140, 16038 Algiers, Algeria; and **Mohamed Trari**, Laboratory of Storage and Valorization of Renewable Energies, Faculty of Chemistry (USTHB), BP 32, 16111 Algiers, Algeria. Contact e-mails: mmehenni@usthb.dz, zlounis@yahoo.com, fatma.ahnia@univ-bejaia.dz, fatmahnia@yahoo.fr, dmiroudlsgm18@gmail.com, amarmanseri@hotmail.com, and solarchemistry@gmail.com.

magnetic and mechanical properties, reducing their service life and performance, as well as limiting their field of application. It is therefore crucial to understand the corrosion mechanisms affecting NdFeB magnets and to develop appropriate protection strategies to preserve their structural and magnetic integrity. In this regard, numerous studies have been conducted to examine the properties of NdFeB magnets (Ref 17-22).

It is essential to separate the Nd₂Fe₁₄B grains from each other to obtain a structure with optimal properties using non-ferromagnetic layers, generally consisting of the Nd-rich phase. It forms during liquid-phase sintering as layers between the grains of Nd₂Fe₁₄B, the thickness of the layers needed for effective magnetic insulation between the grains does not exceed a few nanometres. A high amount of the Nd-rich phase decreases the saturating power of alloys. Therefore, the amount of Nd-rich phase should be as low as possible i.e. at a minimum level necessary for effective magnetic insulation between the grains of the Nd₂Fe₁₄B hard magnetic phase (Ref 23-26). Several effective methods to improve corrosion resistance (Rp) have been developed, and among these alternatives, there is the development of protective coatings (Ref 27-30). Another strategy to improve the properties of NdFeB is to modify the grain boundaries by reconstruction and/or diffusion of other elements, such as Al, Si, Dy-Pr, Ag, Nd-Al-Cu, La-Al-Cu with various Al/Cu ratios, Cu-Zn and Dy₂O₃ powders, Pr-Tb(Cu, Al) alloys as well as rare earths like Tb, Ce and La (Ref 31-40). In this work, we focus on studying the possibility of recycling NdFeB magnets, to improve their vulnerable corrosion resistance, and trying to keep the same others properties. We add a Ni-Cr alloy, specifically a commercial powder called MB40, in various quantities, to improve the corrosion resistance, microstructure and magnetic properties, compared to a starting magnet recovered and used as an initial sample.

2. Materials and Methods

The Nd₂Fe₁₄B magnets chosen in this study were recovered from electronic waste (hard drives); they contain two fragments of horizontal trapezoidal magnet superimposed and covered with a layer of anti-oxidation nickel. The average mass of a magnet contained in a single hard drive is between 3 and 7 g. The Nickel coating was removed after demagnetization of the magnet at the Curie temperature ($T_C = 350$ °C) for a 60 min holding time. Liquid nitrogen embrittlement at 77 K is a process applied to make magnets more brittle for easier grinding. The Nd₂Fe₁₄B magnet was then ground using a RETSCH PM 400 planetary mill equipped with two steel jars and balls. Each jar contains 40 g of material, and the ball-to-material mass ratio was 10:400. The rotation speed was set at 250 rpm, with a 10 min operation time per cycle and 5 min pause time per cycle. This process was repeated for a total of 10 cycles, resulting in a total grinding time of 100 min. At the end of this procedure, a finely ground powder with an average particle size of 95 μ m was obtained (Fig. 1a). This powder was analyzed by SEM and EDX (SI.1 and SI.2), revealing the presence of 59.67 at.% Fe, 32.59 at.% Nd, 05.35 at.% Pr and 06.53 at.% O.

The Malvern HYDRO 2000MU laser particle size analyzer was used to determine the particle size distribution by laser light diffraction. This method relies on the deflection of light rays when they encounter particles suspended in a dispersing

liquid passing through a laser beam. The degree of deviation corresponds to the number and size of particles measured. The device assumes spherical particles with an average radius of 0.05 μ m. The powders analyzed are insoluble in distilled water which was used as a dispersant.

Our samples were doped with two percentages of a commercial Ni-Cr alloy powder (MB40). The MB40 additions to waste powders were set between 0 and 1 wt.% of which 90 % of the grains have a size smaller than 77 μ m (viz., Fig. 1b). The Nd₂Fe₁₄B powder and MB40 powder were physically mixed together in a ball mill for 20 min. This operation had two objectives: to homogenize the powder mixture and to obtain a finer powder by reducing agglomeration. The SEM micrographs in SI.3 revealed the attainment of a finer granulometry. The powder mixture was put into a pressing mold and compacted at a uniaxial pressure of 200 MPa for 65 min under a magnetic orientation field of 159.15 kA.m⁻¹. The compacted samples obtained are cylindrical in shape, with 1.5 cm in diameter and 1.5 cm in thickness.

The green compacts were sintered at the ideal temperature in two stages: an initial homogenization stage at 900 °C for 10 min, followed by a second stage at 1180 °C during 2 h. The heating rate was 10 °C/min. Two annealing processes were then carried out at 700 and 500 °C for 2 and 1 h, respectively (Ref 41, 42), followed by gradual cooling inside the furnace chamber to room temperature (Ref 43). The sintering and annealing processes were carried out in a controlled environment (a vacuum of 0.001 mbar was created inside the furnace chamber, followed by argon gas injection).

Sample preparation is a crucial step in ensuring accurate and reliable results. A resin coating has been applied for easy and efficient sample handling, leaving a bare surface area of 1 cm². All samples: initial, undoped (0 wt.% MB40), 0.5 wt.% and 1 wt.% MB40, were cleaned with ethanol before each test, followed by mechanical polishing with SiC papers (grade 400–1200) and final polishing with diamond paste (1 μ m) to obtain a mirror surface. The tests were carried out under laboratory conditions (25 ± 1 °C).

The SEM experiment was performed by using an ultra-high resolution analytical Schottky field emission scanning electron microscope (FESEM JEOL JSM-7610F Plus) coupled to a Bruker QUANTAX 200 Energy Dispersive x-ray Spectrometer (EDS) system. Optimized quality images were obtained under the following conditions: high vacuum mode (9.6E–5 Pa chamber pressure) of 15 kV accelerating voltage, 85 μ A beam current, and variable magnification. To identify all phases formed during the sintering of our MB40 doped magnet, XRD analysis was carried out with a PIXcelunder X'Pert equipped with Cu-K α radiation.

An electrochemical study was conducted using a PGZ 301-Voltalab 40 Potentiostat controlled by a microcomputer (Volmaster 04 Software). For electrochemical tests, we used open-circuit potential (OCP), Tafel polarization and EIS measurements. These tests were carried out in an aerated 3.5 wt.% aqueous NaCl solution, under ambient conditions, at (25 ± 1) °C and without stirring. All electrochemical tests were carried out in a 100 cm³ thermostatic glass cell with a standard three-electrode system containing Nd-Fe-B magnet as working electrode (10×10 mm²), a saturated calomel electrode (SCE) as reference and Pt-auxiliary electrode. To start the experiments, the sample was introduced into the cell and allowed to reach equilibrium, which typically took about 40 min. The OCP experiment was done for 7200 s. Tafel

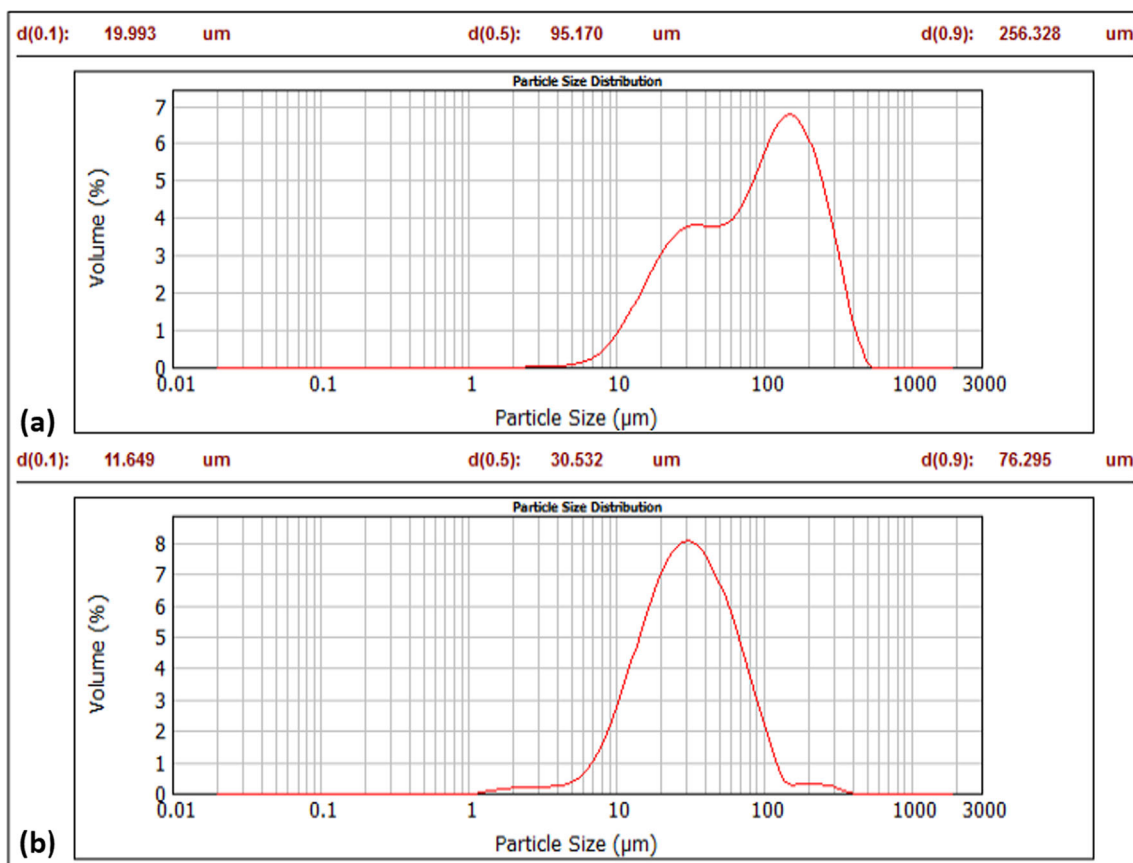


Fig. 1 Powder sizes of (a) recycled $\text{Nd}_2\text{Fe}_{14}\text{B}$ after initial grinding for 100 min., and (b) CrNi doping powder (MB40), analyzed by Laser Granulometry

polarization experiments were performed with a constant scan rate of $10 \text{ mV}\cdot\text{min}^{-1}$ within the range $[-1400 \text{ to } +300 \text{ mV}]$. Semi-logarithmic plots, i.e. $\log(i)$ versus E , are used to determine both the corrosion potential (E_{corr}) and corrosion current (i_{corr}). They were obtained from the plots by using the extrapolation method. The EIS measurements were performed to investigate the corrosion mechanism of recycled NdFeB magnets at a potential amplitude of 10 mV, over a frequency range [100 kHz to 10 mHz].

Magnetic measurements were conducted with a vibrating sample magnetometer (VSM) with a sensitivity of 10^{-5} emu (Microsense EZ9 brand). Calibration was carried out at 300 K, using a 99.99 % pure nickel sample with a standard magnetization value of 54.9 emu/g. Vickers Hardness was evaluated using a Wilson TUKONTM (TM superscript) 1202 micro-durometer. For each sample (initial, undoped, 0.5 and 1 wt.% MB40), we carried out four (04) tests and calculated the average, using a standard charge of 50 kgf with a measured standard deviation of 8.32 and at a temperature of $25 (\pm 1) \text{ }^\circ\text{C}$. Surface preparation was the same as described for electrochemical testing, including cleaning and polishing. To ensure the integrity of the results, the sample was securely fixed during testing.

3. Results and Discussion

SEM images of the four samples before electrochemical experiments are shown in Fig. 2: initial and recycled (undoped, 0.5, and 1 wt.% MB40 additives). We observe a typical grain distribution, characteristic of a sintered material (Fig. 2a-d). The dark gray region corresponds to the $\text{Nd}_2\text{Fe}_{14}\text{B}$ matrix phase (viz., Fig. 3, spectrum 1), while the light region is that of the Nd-rich intergranular phase (Fig. 3, spectrum 4) (Ref 31), as confirmed by the EDS analysis. In the case of the initial magnet (viz., Fig. 2a), the Nd-rich phase tends to aggregate at grain junctions, leading to a reduction in Nd-rich continuous layers to fully isolate $\text{Nd}_2\text{Fe}_{14}\text{B}$ grains (Ref 8, 23, 40, 44).

The undoped magnet (viz., Fig. 2b) exhibits the same structural configuration but with fewer visible defects at the grain boundaries, compared to the initial magnet. An increase in the MB40 concentration from 0.5 to 1 wt.% (viz., Fig. 2c, d) leads to the formation of Nd, Ni, and Cr-rich phase between adjacent grains. The intergranular phase then becomes more distinct and elongated, due to the enhanced fluidity of the Nd-rich phase during the sintering and annealing processes (Ref 23). The inclusion of 1 wt.% MB40 not only enhances the microstructure of the $\text{Nd}_2\text{Fe}_{14}\text{B}$ magnet but also alters the composition of the intergranular phase. A multipoint Energy-dispersive x-ray spectroscopy analysis (EDS) was performed and reported in Fig. 3. The overall composition of the Nd-Fe-B matrix phase remains consistent as depicted in Fig. 3 (spectrum 1). The appearance of an iron agglomeration in the form of a

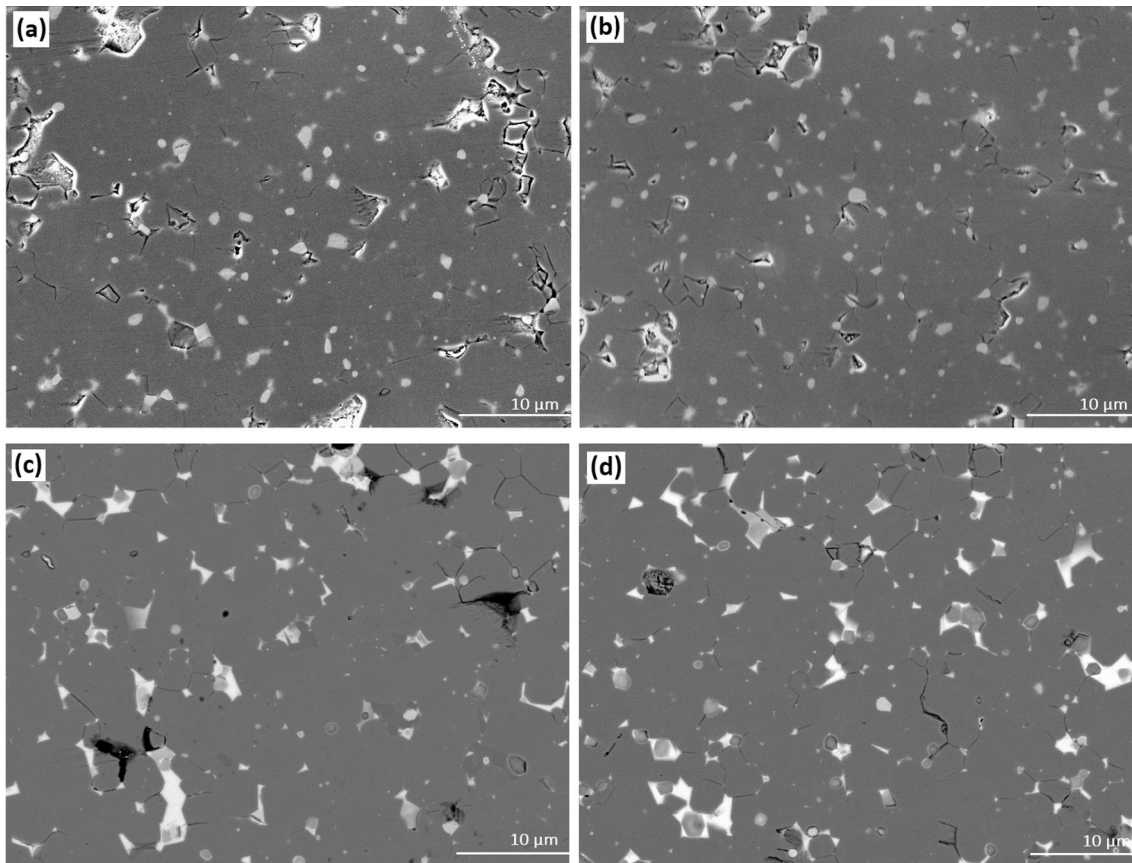


Fig. 2 SEM back-scattered images of: (a) initial $\text{Nd}_2\text{Fe}_{14}\text{B}$ sample, (b) undoped, (c) 0.5 wt.% MB40 addition, and (d) 1 wt.% MB40 addition

black spot can be attributed to the formation of $\alpha\text{-Fe}$ during sintering, as illustrated in Fig. 3 (spectrum 2). In the grain boundary regions of the magnet, two distinct regions are evident: Ni-Cr-Fe (Fig. 3, spectrum 3) and Nd-rich (Fig. 3, spectrum 4). Ni-Cr-Fe results from the reaction between MB40 additives and Fe during the sintering process. It is evident that Ni and Cr diffused into the intergranular phase (Fig. 3, spectrum 3), thereby decreasing the amount and penetration of Nd in this region.

We observe that the majority $\text{Nd}_2\text{Fe}_{14}\text{B}$ phase corresponds to the dark gray region. A second phase was revealed (Fig. 3, spectrum 2), which corresponds to $(\text{Nd,Pr})_{1+\alpha}\text{Fe}_4\text{B}_4$. This observation is consistent with the coexistence of Nd and Pr in EDX analysis of $\text{Nd}_2\text{Fe}_{14}\text{B}$ magnets, as Pr consistently appears with Nd due to their proximity in the periodic table. The presence of the $(\text{Nd, Pr})_{1+\alpha}\text{Fe}_4\text{B}_4$ phase is therefore estimated in relation to the presence of Pr, Nd and Fe (SI.2), this phase was already reported by *Givord* (Ref 44). Its presence is confirmed in XRD measurements of the sintered magnet doped with 1 wt.% MB40. As noted, Cr is an alpha genic element that facilitates the generation of $\alpha\text{-Fe}$, known for its ferromagnetic properties at low temperatures (950 °C). The multi-material compound we developed contains 6 elements namely Fe, Nd, Pr, B, Cr and Ni distributed in 6 phases: $\text{Nd}_2\text{Fe}_{14}\text{B}$, $(\text{Nd,Pr})_{1+\alpha}\text{Fe}_4\text{B}_4$, Nd-rich, $\alpha\text{-Fe}$, NiCrFe and $\text{Fe}_1\text{Ni}_4\text{Nd}_1$. In this case, the comparison of the standard potential is not sufficient to prejudge the electrochemical behavior. Figures 2 and 3 clearly demonstrate the effectiveness of the grinding method. The presence of Si, N, and C elements in the EDX analysis spectrums is primarily attributed to contamination.

Among the corrosion control methods, electrochemical analysis is of great importance for understanding the phenomenon through the information they provide. Their advantage lies in the fact that it is possible to carry out tests in a few hours. The principle is based on measuring the current (i) passing through the electrode as a function of the potential (E) applied.

Figure 4 depicts the OCP progression of $\text{Nd}_2\text{Fe}_{14}\text{B}$ magnets doped with MB40, in 3.5 wt.% NaCl aqueous solutions, which changes with the nature of the magnet. This represents the variation of the corrosion potential, also called abandonment potential, over time. The shape of the curves shows that the dissolution mechanisms are identical for the four samples. However, a slight attack is observed, indicating the formation of an oxide layer. The curve at 1 wt.% (green line) shows the destruction of a layer, probably the sesquioxide Cr_2O_3 , explaining the cathodic shift (-560 mV). The starting potential of the sample doped with 1 wt.% MB40 is equal to -415 mV and begins to decrease, reaching a value of -555 mV after 13 min. A slower decrease is observed during 17 min to reach a value of -560 mV. At $t = 35$ min; $E = -559$ mV, an increase in potential is observed. After 110 min, the potential shifts to positive values before stabilizing at a level ranging from -490 to -495 mV for the remainder of the experiment. On the other hand, the initial, undoped, and 0.5 wt.% MB40 curves indicate a continuous and spontaneous dissolution followed by stabilization after 50 min. At the beginning ($t_0 = 1$ s), the potential of the initial sample is equal to -689 mV and decreases to stabilize at -717 mV after 20 min of immersion. The undoped sample exhibits the

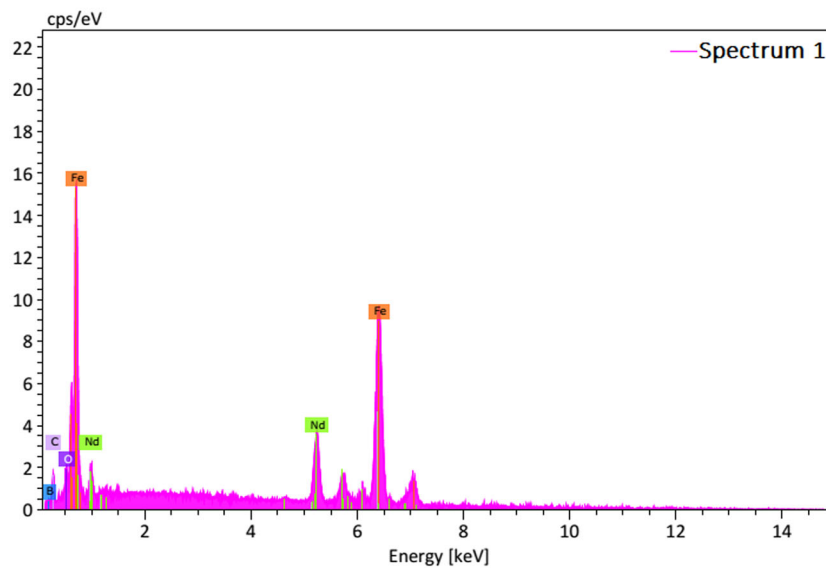
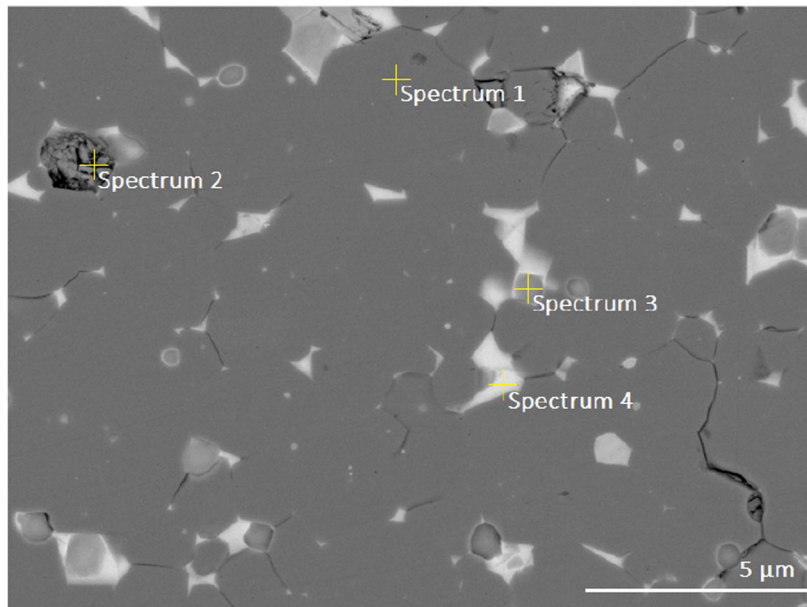


Fig. 3 BSE-SEM image and EDS spectrum (1, 2, 3 and 4) of spatial distribution of Fe, Nd, Ni and Cr across the matrix phase and intergranular phase in the 1 wt.% MB40-doped magnet

same process, with a potential starting at -665 mV and stabilizing at -682 mV after 14 min. The 0.5 wt.% doped magnet starts at -557 mV and reaches a potential of -592 mV after 20 min of immersion. Taking into account the standard potentials of Nd (-2.32 V) and Cr (-0.74 V), we can conclude that the formation of a protective layer composed mainly from Nd_2O_3 (without discarding the Cr_2O_3 which appears on the XRD pattern). Based on the “Potential-pH” diagram, a pH of 6.7 favors the formation of Nd_2O_3 . Indeed, oxidation of the Nd-rich phase in NdFeB can be advantageous, thereby improving corrosion resistance through the reduction of the marginal Nd-rich layer. Therefore, the corrosion resistance of the sample increases with Nd_2O_3 (Ref 7).

Due to the overlap of certain parts of the semi-logarithmic curves, we chose to separate the plots. The curves clearly show an active region corresponding to the Nd-rich phase. The polarization curve allows us to access the current density $\log(i)$

and the polarization resistance (R_p). We observe a similarity in the evolution of the current as a function of the potential (E). The four curves represent three stages: the first one is due to rapid charge transfer. The second stage is the mixed regime, and the final stage is the diffusion initiation where the intensity increases significantly with potential. Figure 5 shows that the doped samples, (0.5 and 1 wt.% MB40), exhibit lower corrosion intensities. The doped samples containing 0.5 and 1 wt.% MB40 exhibit more positively shifted E_{corr} ranging from -734 to -696 mV, respectively, compared to the initial sample, which varies between -782 and -826 mV. Furthermore, the current i_{corr} ranges from 0.25 to $0.2 \mu\text{A}\cdot\text{cm}^{-2}$ for 0.5 and 1 wt.% MB40, respectively, compared to the initial sample and the undoped sample, equal respectively to 0.218 and $0.17 \text{ mA}\cdot\text{cm}^{-2}$. All these data are compiled in Table 1, where we notice that the increase in E_{corr} is proportional to the MB40 doping rate, indicating primarily a change in the potential of grain boundaries.

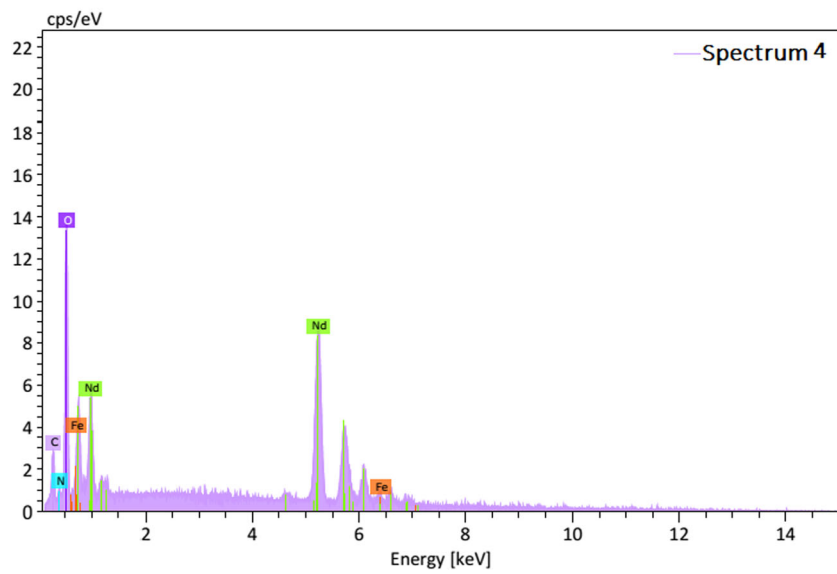
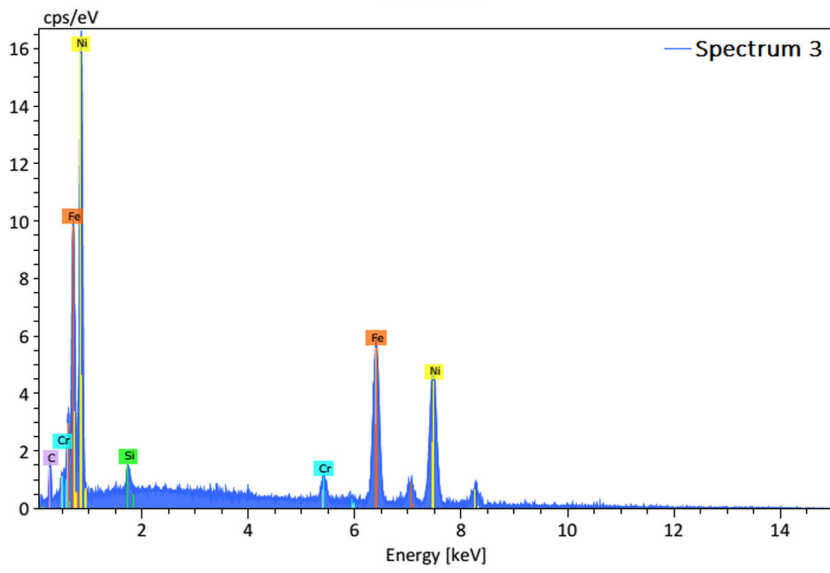
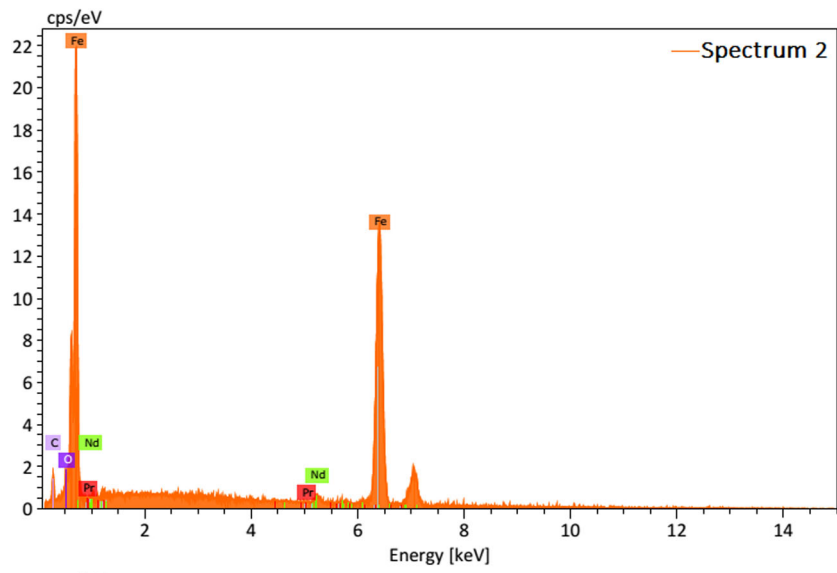


Fig. 3 continued

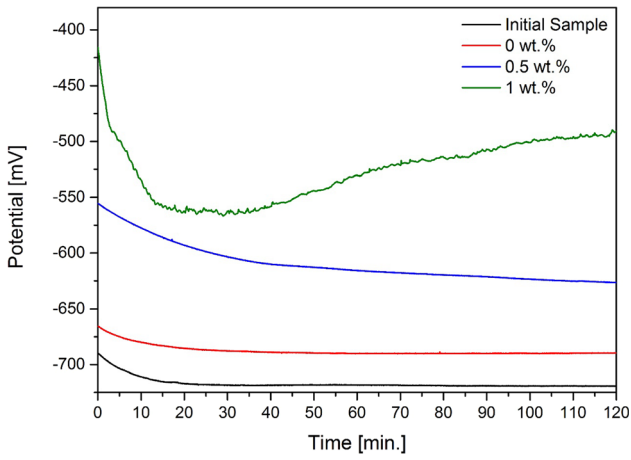


Fig. 4 Evolution of the Open Circuit Potential (OCP) for the $\text{Nd}_2\text{Fe}_{14}\text{B}$ magnet as a function of MB40 contents in 3.5 wt.% NaCl aqueous solutions

We observe that the anodic branches are parallel, which characterizes the same mechanism. The increase in current density is low, a behavior probably associated with the heterogeneity of the oxide layer formed. Figure 6(a) and (b) shows the evolution of i_{corr} , E_{corr} , R_p and corrosion rate (V_{corr}) as a function of Nd-Fe-B samples. Figure 6(a) illustrates the changes in E_{corr} and i_{corr} with respect to the MB40 doping rate. The E_{corr} increases from -826 mV in the undoped sample to -696 mV in the 1 wt.% sample as the MB40 content in NdFeB increases. Simultaneously, i_{corr} exhibits a variation, starting at $0.17 \mu\text{A}\cdot\text{cm}^{-2}$ for the undoped sample (0 wt.% MB40), and increases to $0.25 \mu\text{A}\cdot\text{cm}^{-2}$ when we doped 0.5 wt.% MB40, and subsequently decreasing to $0.2 \mu\text{A}\cdot\text{cm}^{-2}$ when the doping rate reaches 1 wt.% MB40. Meanwhile, R_p improves from 938.9 to $1151.2 \Omega\cdot\text{cm}^2$, respectively, for the initial sample and the 1 wt.% MB40 sample (Fig. 6b). The calculations show that the recycled samples have better R_p values than the initial sample, as well as a corrosion rate which varies between $4.72 \mu\text{m}\cdot\text{year}^{-1}$ for the initial sample and

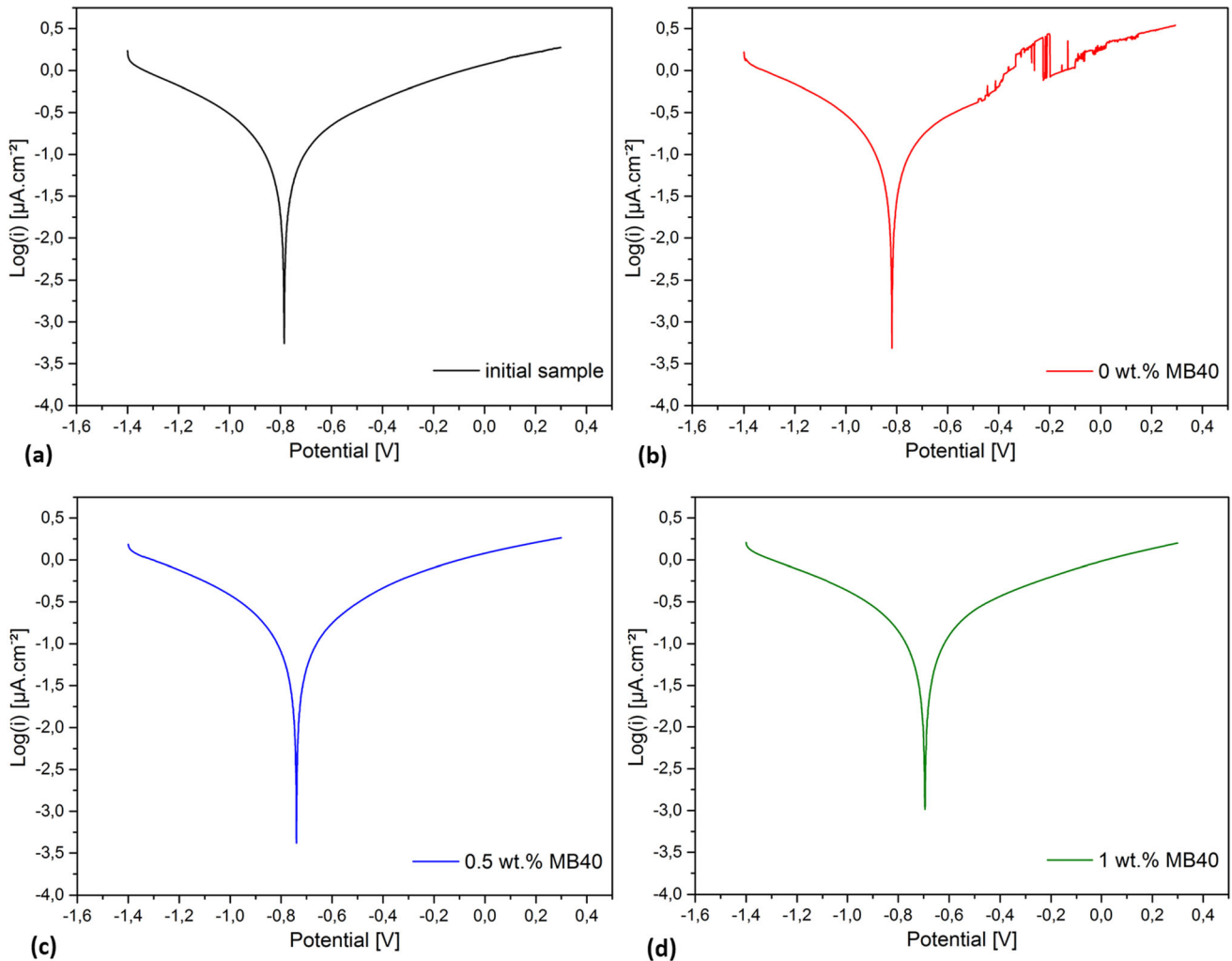


Fig. 5 Potentiokinetic polarization curves of: (a) initial sample, (b) undoped sample, (c) 0.5 wt.% MB40, and (d) 1 wt.% MB40 in 3.5 wt.% NaCl aqueous solution

Table 1 Electrochemical parameters calculated from the potentiodynamic polarization curves in 3.5 wt.% NaCl aqueous solution

	E_{corr} , mV	i_{corr} , $\mu\text{A}\cdot\text{cm}^{-2}$	R_p , $\Omega\cdot\text{cm}^2$	V_{corr} , $\mu\text{m}\cdot\text{year}^{-1}$
Initial sample	- 782	0.218	938.9	4.72
0 wt.% MB40	- 826	0.17	929.7	3.69
0.5 wt.% MB40	- 734	0.25	826.2	5.43
1 wt.% MB40	- 696	0.2	1151.2	4.34

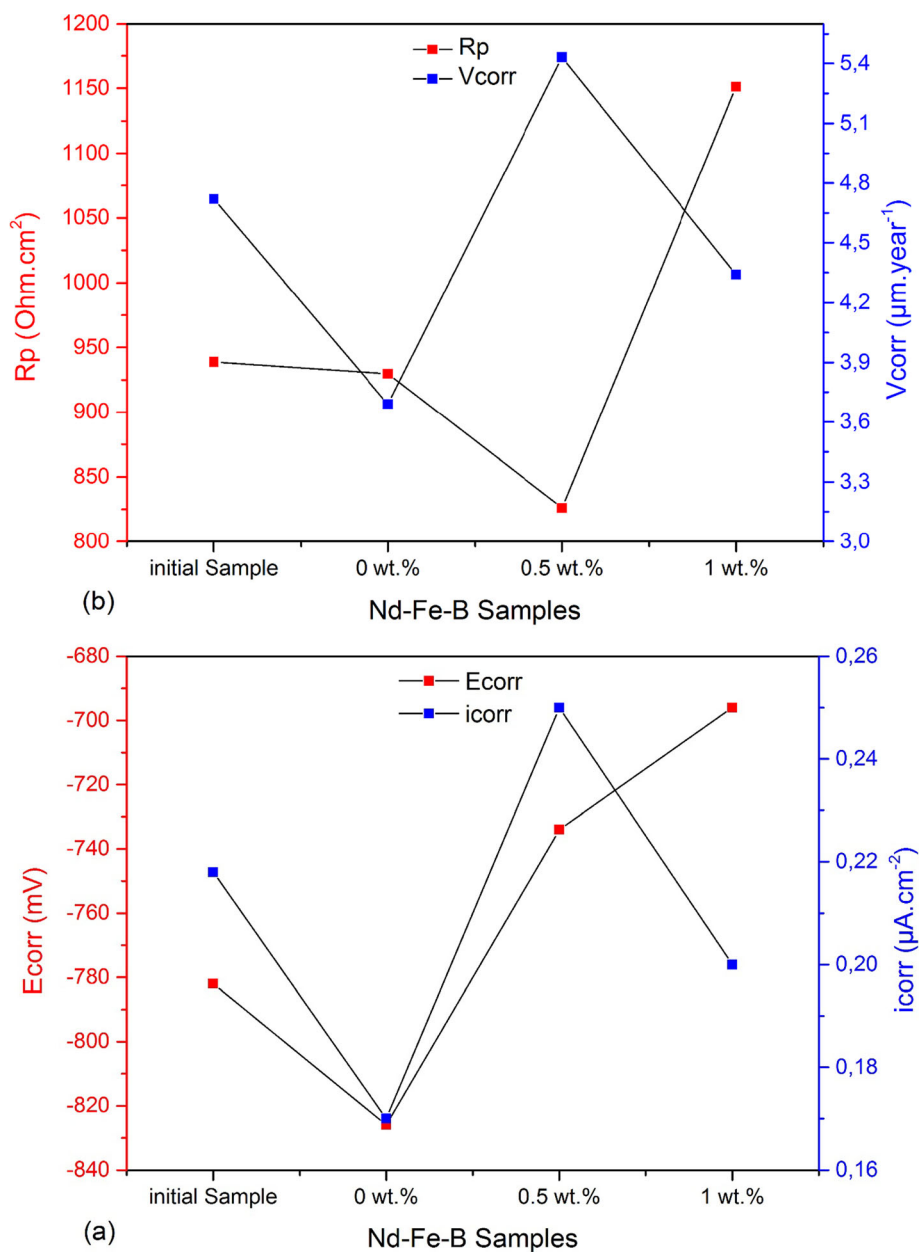


Fig. 6 The evolution of: (a) $E_{\text{corr}} / i_{\text{corr}}$ and (b) V_{corr} / R_p as a function of $\text{Nd}_2\text{Fe}_{14}\text{B}$ samples

4.34 $\mu\text{m}\cdot\text{year}^{-1}$ for the 1 wt.% MB40 doped sample. The best E_{corr} and R_p values are attributed to the 1 wt.% MB40 doped sample. The differences observed in R_p and V_{corr} among the initial, undoped, 0.5 and 1 wt.% MB40 can be attributed to the concentration and reaction rate of Cr, Ni, and C. This presence reflects the formation of the corrosion product (the Nd_2O_3 layer

in both initial and undoped samples, and $\text{Nd}_2\text{O}_3 + \text{Cr}_2\text{O}_3$ in the 1 and 0.5 wt.% MB40 sample). Even in very low amounts, the chromium and carbon contained in NdFeB can have an influence comparable to that observed in stainless steels, affecting corrosion resistance through improvement or deterioration. Compared to the electrochemical results reported by

Popescu et al. (Ref 7) and Wu et al. (Ref 18), our recycled magnet achieves excellent results with higher R_p and lower V_{corr} .

The lack of Fe_2O_3 and $Fe(OH)_3$ is highlighted by EDS Spectrum (Fig. 3) and XRD analysis, which shows the formation of the non-porous Nd_2O_3 layer that makes O_2 diffusion difficult. Back-scattered SEM images of the $Nd_2Fe_{14}B$ doped with 1 wt.% MB40 after electrochemical test (SI.4) revealing the formation of the Nd_2O_3 corrosion layer at different scales: (a) at 150 X magnification, (b) at 500 X magnification. We note the absence of microporosities and that corrosion appears uniformly on the surface of the sample. The R_p values allow us to claim that our multi-material has a good corrosion resistance. The micrographs reveal also no pitting corrosion due to the presence of chloride.

Figure 7 illustrates the EIS plots of imaginary impedance (Z'') as a function of real impedance (Z') for each polarization frequency obtained from NdFeB magnets (initial, undoped, doped with 0.5, and 1 wt.% MB40). The impedance plots show capacitive loops, indicating that all the samples have the same corrosion mechanisms. The diameters of the capacitive loops of the samples doped with 0.5 and 1wt.% MB40 are larger than those of the initial and the undoped samples.

It is observed that in the high-frequency region of the impedance diagram, the capacitive loop is not centered on the real axis. This allows us to state that the model include a constant phase element (CPE) which explains the deviation from pure capacitive behavior. In the high-frequency part, we have a charge transfer, whereas in the second part, a double layer is expressed by the reaction (1). So, the negative and positive charges represent the double layer. The initiation of the formation of the oxide layer of Nd_2O_3 (reaction (2)) referring to the calculated Pilling-Bedworth ratio (R_{PB}) of Nd_2O_3 , which is equal to 1.12. It provides an additional segment of the diagram, specifically related to the low-frequency range, illustrating the diffusion of oxygen through the oxide layer formed. This phenomenon is correlated with the redox reactions occurring within the film. The doped samples (0.5 and 1 wt.% MB40) exhibit identical behavior. The calculated thickness of the oxide layer formed (Nd_2O_3) in the 1 wt.% MB40 sample is $d = 8.2 \mu m$ by using Eq 3.

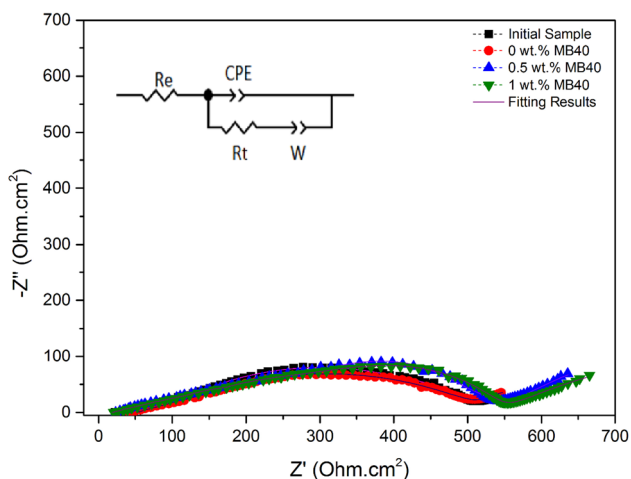


Fig. 7 Nyquist diagrams and the proposed equivalent circuit of: initial sample, undoped $Nd_2Fe_{14}B$ and doped $Nd_2Fe_{14}B$ with 0.5 and 1 wt.% MB40 in 3.5 wt.% NaCl aqueous solutions



Electrical circuits can be employed to compute kinetic constants or forecast the progression of impedance diagrams. The Electrochemical Impedance Spectroscopy (EIS) diagrams demonstrate frequency dispersion, characterized by capacitance variation expressed in terms of Constant Phase Element (CPE) (Ref 21, 26). The equivalent electrical circuit (Fig. 7), modeling this type of interface, was obtained after fitting the data with the ZSimpWin program. We selected the sample exhibiting optimal electrochemical parameters (1 wt.% MB40) for modeling the equivalent circuit in our study. We adopted the Randles model, which is the oldest model developed to simultaneously characterize the various static and dynamic aspects of an electrochemical cell. Considering the explanations provided earlier, our proposed model is composed of the following elements:

- The resistance R_e corresponds to the electrolyte resistance.
- The resistance R_t corresponds to the charge transfer resistance.
- The capacitor (CPE) which models the electrical double layer phenomenon at the corrosion product/matrix interface.
- The impedance W is indicative of diffusion under Warburg boundary conditions. It represents diffusion control and is incorporated into the circuit in series with the charge transfer resistance (R_t) (Ref 45). The diffusion control is manifested as a linear segment at the end of the capacitive arc, inclined at 45° from the real axis. If α is close to 0.5 then the CPE is a Warburg impedance.

$$C_{dl} = \frac{\gamma \times \gamma_0 \times S}{d} \quad (\text{Eq 3})$$

where:

- C_{dl} : is the double layer capacitance,
- γ : is the Nd_2O_3 dielectric constant,
- γ_0 : is the vacuum permittivity,
- S : is the sample surface,
- d : is the thickness of Nd_2O_3 layer.

In this experiment, CPE, W , R_e and R_t values of the sample doped with 1 wt.% MB40 are listed in Table 2. Initially, we have R_e , from the start of the experiment, the curve starts from the ohmic drop deduced from the EIS graph at the zero ordinate (0). Then, by disturbing the system with a pulse, a current is generated which reflects a transfer of charge. Due to the disturbance observed on the diagram, the R_t value is difficult to read, so we referred to the Bode diagram. Calculating the CPE would make it possible to propose an equivalent circuit taking into consideration the high frequency domain, the resistance of

Table 2 Equivalent circuit model parameters proposed of the sample doped with 1 wt.% MB40

$R_e, \Omega.cm^2$	$CPE_{dl}, \Omega^{-1}.cm^{-2}.s^n$	$R_t, \Omega.cm^2$	$W, \Omega^{-1}.cm^{-2}$
18	1.21E-5	588.9	8.5E-2

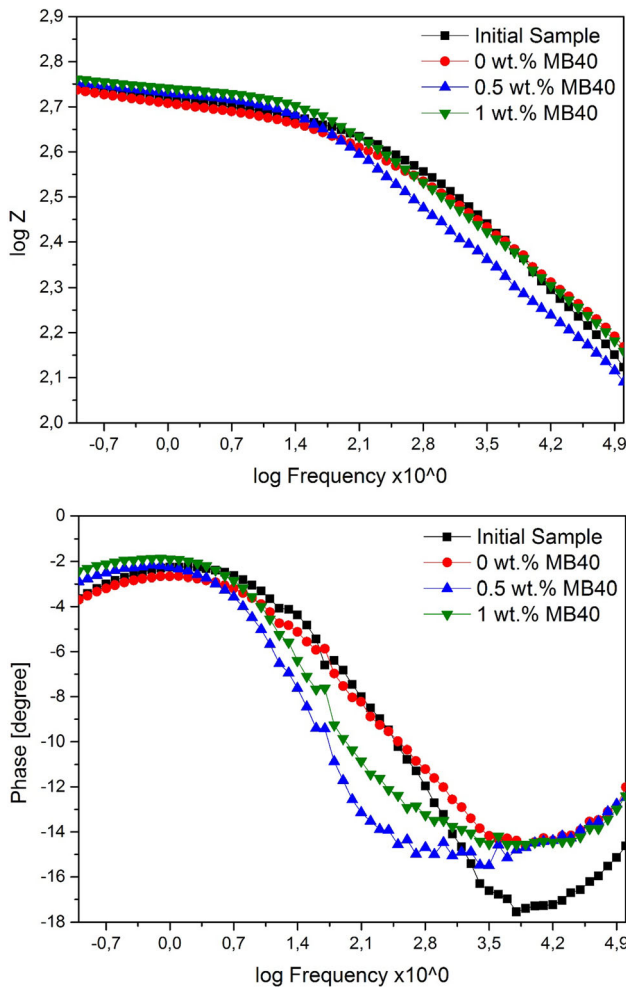


Fig. 8 Bode (impedance and phase shift) plots for: initial sample, undoped sample, 0.5 wt.% MB40, and 1 wt.% MB40

the electrolyte R_e , the faradic impedance, including the resistance to charge transfer, and the double layer capacitance. The oxide film produced between substrate and electrolyte is similar to an electrical double layer, which is referred to as a constant-phase element (CPE) in the equivalent circuit (Fig. 7) (Ref 45).

The Bode plots i.e. $\log Z$ as a function of \log frequency (Fig. 8), show that we are dealing with a single time constant ($\alpha = 0.34$) which confirms the Warburg impedance where the modeling includes only one CPE. It's clear that impedance and phase shift values depend not only on frequency, but also on the MB40 doping rate. At high frequencies, such as 100 kHz, impedance and phase shift increase from around $133 \Omega\text{-cm}^2$ with -14.63° to $144 \Omega\text{-cm}^2$ with -12.4° after the addition of 1 wt.% MB40 doping. Using Eq 4, the calculated Pilling-Bedworth ratio (R_{PB}) is equal to 1.12. This value is comprised between 1 and 2, so the Nd_2O_3 oxide film acts as a protective layer on the surface of our substrate.

$$R_{PB} = \frac{M_{\text{oxide}} \times \rho_{\text{metal}}}{n \times M_{\text{metal}} \times \rho_{\text{oxide}}} \quad (\text{Eq 4})$$

where:

- M : atomic or molecular mass,

- n : number of atoms of metal per molecule of the oxide,
- ρ : density,
- V : molar volume.

The diffusion and oxidation processes are too complex when we are dealing with two oxidation layers (Nd_2O_3 and Cr_2O_3). However, the only time constant that appears in the Bode curve is attributed to the dominant Nd_2O_3 layer, as confirmed by Pilling Bedworth report.

To identify the phase composition of the magnets and clarify the influence of MB40 on the microstructure, XRD analysis was performed for the initial $\text{Nd}_2\text{Fe}_{14}\text{B}$ magnet and for the recycled magnet with 1 wt.% MB40 added, which shows the highest corrosion resistance compared to the other samples. The pattern (Fig. 9) shows peaks of the hard magnetic phase $\text{Nd}_2\text{Fe}_{14}\text{B}$, as well as those of the ferromagnetic phases $\text{Nd}_1\text{Fe}_4\text{B}_4$ and $\alpha\text{-Fe}$. Compared to the pattern of the initial NdFeB , 1 wt.% doped sample, shows mainly the peaks of the hard magnetic $\text{Nd}_2\text{Fe}_{14}\text{B}$ phase, in particular, the characteristic peak at $2\theta = 44.5^\circ$ (Ref 17, 40, 41). Furthermore, intensive grinding and plastic deformation of the crystalline Nd-Fe-B alloy produced a nanocrystalline Fe phase coexisting with an amorphous phase rather than a single amorphous phase. This was demonstrated previously where the authors showed the formation of the tetragonal phase $\text{Nd}_2\text{Fe}_{14}\text{B}$ according to the JCPDS N°98-060-2637 and cubic $\alpha\text{-Fe}$ phase (JCPDS N°98-015-9352). Other phases appear due to 1 wt.% MB40 doping such as the hexagonal $\text{Fe}_1\text{Ni}_4\text{Nd}_1$ phase ($2\theta = 20^\circ, 30.2^\circ, 47^\circ$ and 49° ; JCPDS N°98-010-3551), tetragonal $\text{Nd}_1\text{Fe}_4\text{B}_4$ phase ($35.5^\circ, 37.9^\circ$ and 40° ; JCPDS N° 00-038-0920) and cubic NiCrFe phase ($44^\circ, 65^\circ$ and 82° ; JCPDS N°00-035-1375) (Ref 40). The corrosion products, Nd_2O_3 (JCPDS N°98-010-0207) and Cr_2O_3 (JCPDS N°98-017-3470), are observed in the XRD pattern of the recycled magnet doped with 1 wt.% MB40.

Figure 10 shows the XRD pattern of the MB40 doping powder used as a grain boundary modifier where all peaks of $\text{Cr}_{1.12}\text{Ni}_{2.88}$ face-centered cubic phase are clearly visible at 2θ ($44,28^\circ; 51,59^\circ; 75,97^\circ; 92,38^\circ$ and $97,83^\circ$) in agreement with the JCPDS N°03-065-5559. Additionally, the peaks of the tetragonal CrFe phase were also observed at 2θ ($= 36,8^\circ; 39,9^\circ; 42,31^\circ; 46,23^\circ; 46,9^\circ; 51,76^\circ; 92,56^\circ$ and $98,12^\circ$) (JCPDS N°03-

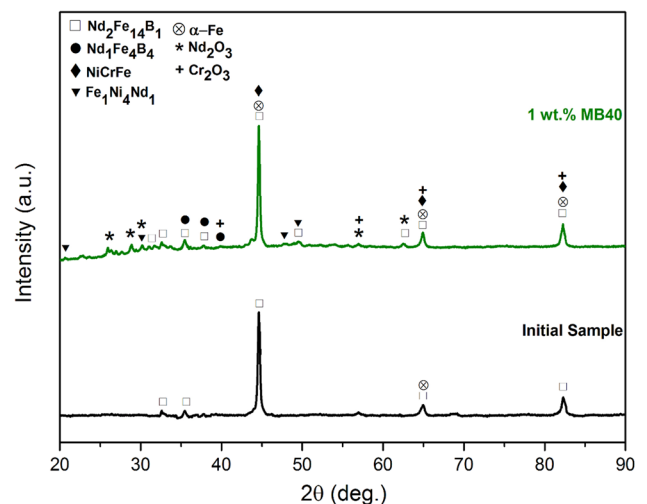


Fig. 9 XRD measurements of the initial $\text{Nd}_2\text{Fe}_{14}\text{B}$ magnet and the sintered magnet doped with 1 wt.% MB40

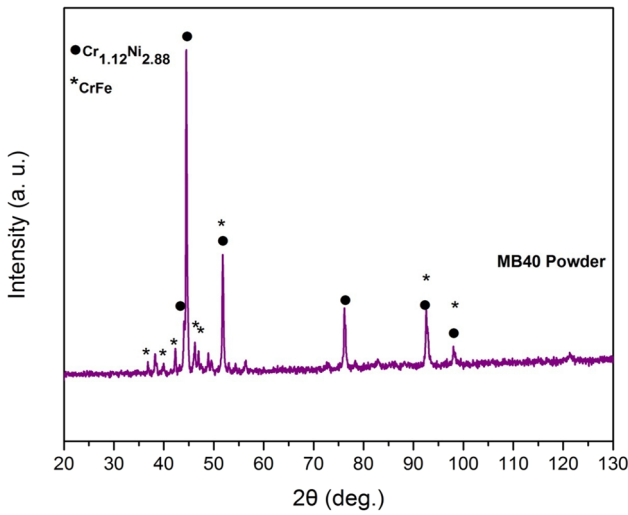


Fig. 10 XRD of the MB40 (Ni-Cr alloy) doping powder

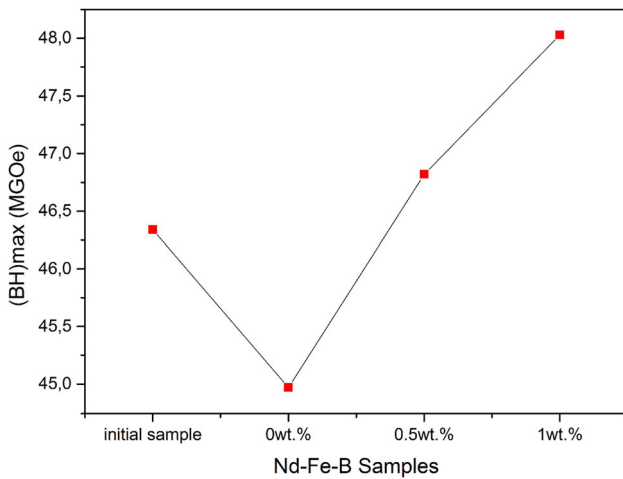


Fig. 11 The maximum energy product $(BH)_{\max}$ of $Nd_2Fe_{14}B$ magnets with different MB40 contents: initial, undoped, 0.5 and 1 wt.%)

065-4528). The addition of NiCr confers a strong magnetization which persists through the phenomena of magnetic hysteresis illustrating remanence.

The maximum energy product $(BH)_{\max}$ of $Nd_2Fe_{14}B$ samples with different MB40 contents (initial, 0, 0.5 and 1 wt.%) is illustrated in Fig. 11. The coercive field (H_c), saturation magnetization (B_s), remanence (B_r) and energy product $(BH)_{\max}$ are listed in Table 3. All samples exhibit magnetic behavior characteristic of hard materials. We ob-

Table 3 Magnetic properties of the experimental Nd-Fe-B samples

	B_s , T	B_r , T	H_c , kOe	$(BH)_{\max}$, MGOe
Initial sample	2.12	1.08	9.8	46.34
0 wt.% MB40	1.93	0.99	8.19	44.97
0.5 wt.% MB40	2.26	1.17	10.5	46.82
1 wt.% MB40	2.58	1.32	10.8	48.03

served that B_s decreases from the initial sample to the undoped sample (0 wt.% MB40) from 2.12 to 1.93 T, respectively. However, samples doped with 0.5 and 1 wt.% MB40 showed an increase in magnetization, respectively, from 2.26 to 2.58 T. The parameter B_r follows a similar trend, decreasing from 1.08 to 0.99 T respectively for the initial sample and the undoped sample, while the 0.5 and 1 wt.% MB40 samples showed an increased remanence equal to 1.17 and 1.32 T, respectively. Magnetic measurements also indicated variations in coercivity (H_c) with values of 9.8, 8.19, 10.5, and 10.8 kOe for the initial sample, 0, 0.5, and 1 wt.% of MB40, respectively. An improved energy product $(BH)_{\max}$ is observed for the sample doped with 0.5 and 1 wt.% MB40, equal to 46.82 and 48.03 MGOe, respectively. However, the undoped sample shows slightly lower energy production, equal to 44.97 MGOe, compared with the initial sample at 46.34 MGOe. Therefore, doping MB40 can enhance the hard magnetic properties of recycled NdFeB magnets.

Hardness values for initial and recycled NdFeB samples are shown in Fig. 12. We observed a slight increase in hardness for 0.5 and 1 wt.% MB40. For the initial and the undoped samples, the average value varies between 565.2 and 553.7 HV, resp., while 0.5 and 1 wt.% MB40 have slightly higher values of 587.3 and 587 HV, respectively. NdFeB magnets exhibit fracture behavior characterized by intergranular cracking. Fractures initiate and propagate mainly along the brittle boundaries of $Nd_2Fe_{14}B$ grains. This brittle fracture mode is typically observed in NdFeB magnetic materials. Within two-phase NdFeB magnets, the $Nd_2Fe_{14}B$ matrix phase demonstrates greater strength and brittleness compared to the Nd-rich phase (Ref 34). Thus, a proportional relationship between the MB40 doping rate and the hardness of our recycled rare-earth magnets was observed. This is attributable to the modification of the intergranular phase by promoting the diffusion of MB40 and decreasing the infiltration rate of Nd in this region, as well as the formation of new phases such as NiCrFe and $Fe_1Ni_4Nd_1$ alongside the hard $Nd_2Fe_{14}B$ phase and the $Nd_1Fe_4B_4$ phase. This gives our recycled, MB40 doped magnet a higher hardness than the starting (initial) sample.

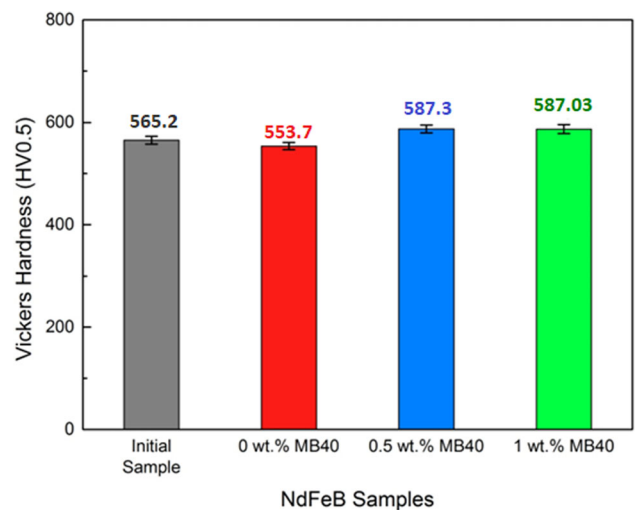


Fig. 12 Hardness measurements of $Nd_2Fe_{14}B$ magnets: initial sample, undoped, 0.5 and 1wt.% MB40 with corresponding standard deviations

4. Conclusion

In this work, we focused on adding MB40 powder to the intergranular phase of sintered Nd₂Fe₁₄B magnets. This resulted in exceptional magnetic and structural characteristics, as well as excellent corrosion resistance. This improvement is attributable to the increase in the electrochemical potential of the intergranular phase. The addition of 0.5 and 1 wt.% MB40 to the Nd₂Fe₁₄B matrix has a favorable effect on electrochemical behavior, in particular, NdFeB phase potential and Nd-rich grain boundaries. The sample, doped with 1 wt.% MB40, exhibits higher polarization resistance and a lower corrosion rate than the initial sample during the corrosion process in NaCl aqueous solutions. This was due to the formation of the Nd₂O₃, known as the corrosion product of the Nd-rich phase on the doped magnet surface. XRD analysis confirmed the formation of specific phases such as NiCrFe, Fe₁Nd₁Ni₄ and Nd₂O₃ which optimize the electrochemical and magnetic properties, homogeneity and hardness of the microstructure. Using Ni-Cr alloy (MB40) to modify grain boundaries represents a promising approach to forming Nd₂Fe₁₄B magnets that effectively resist corrosion and produce more efficient magnetic energy (remanence and coercivity), while reducing the amount of expensive rare earths. More importantly, this change also helps protect the environment by promoting the recycling of electronic waste, including hard drives. This is an ambitious step towards a more sustainable and environmentally friendly magnet industry.

Acknowledgments

The authors thank the University of Sciences and technology of Houari Boumediene (Algeria).

Data availability

The authors declare that they have no known competing financial interest or personal relationships that could have appeared to influence the work reported in this paper.

References

1. X. Xu, S. Khoshima, M. Karajic, J. Balderman, K. Markovic, J. Scancar, Z. Samardzija, S. Sturm, and K.Z. Rozman, Electrochemical Routes for Environmentally Friendly Recycling of Rare-Earth-Based (Sm-Co) Permanent Magnets, *J. App. Electrochem.*, 2022, **52**, p 1081–1090
2. S. An, Z. Ma, W. Li, H. Zhang, and T. Yan, Magnetic Properties of Anisotropic Bonded NdFeB/SmCo Permanent Magnets, *J. Ame. Instit. Phys. Adv.*, 2019, **9**, p 125146–125152
3. T. Elwert, D. Goldmann, F. Roemer, and S. Schwarz, Recycling of NdFeB Magnets from Electric Drive Motors of (hybrid) Electric Vehicles, *J. Sustain. Metall.*, 2017, **3**, p 108–121
4. M. Sagawa and Y. Une, Chapter 5-The Status of Sintered NdFeB Magnets, *Mod. Per. Magn.*, Woodhead Publishing Series, 2022, p 135–168
5. P. Friebe, Development of a Prototype Shredder for WEEE Equipped With NdFeB Magnets, *Min. Mach.*, 2023, **41**(2), p 143–157
6. D.D. München and H.M. Veit, Neodymium as the Main Feature of Permanent Magnets from Hard Disk Drives (HDDs), *J. Waste Manag.*, 2017, **61**, p 372–376
7. A.M. Popescu, J.M. Calderon-Moreno, K. Yanushkevich, A. Aplevich, O. Demidenko, E.I. Neacsu, and V. Constantin, Corrosion Behavior of NdFeB Magnets in Different Aqueous Solutions, *J. Braz. Chem. Soc.*, 2023, **00**, p 1–12
8. A. Kumari, Dipali, N.S. Randhawa, and S.K. Sahu, Electrochemical Treatment of Spent NdFeB Magnets in Organic Acid for Recovery of Rare Earths and Other Metal Values, *J. Clean. Prod.*, 2021, **309**, p 127393
9. A. Lixandru, P. Venkatesan, C. Jönsson, I. Poenaru, B. Hall, Y. Yang, A. Walton, K. Güth, R. Gauß, and O.G. Gutfleisch, Identification and Recovery of Rare-Earth Permanent Magnets from Waste Electrical and Electronic Equipment, *J. Waste Manag.*, 2017, **68**, p 482–489
10. E.E. Kaya, O. Kaya, S. Stopic, S. Gürmen, and B. Friedrich, NdFeB Magnets Recycling Process: An Alternative Method to Produce Mixed Rare Earth Oxide from Scrap NdFeB Magnets, *J. Met.*, 2021, **11**, p 716–729
11. S. Stopic, B. Polat, H. Chung, E. Emil-kaya, S. Smiljanic, S. Gürmen, and B. Friedrich, Recovery of Rare Earth Elements through Spent NdFeB Magnet, *J. Met.*, 2022, **12**, p 1464–1476
12. H. Gagarin and R.G. Eggert, Measuring Trade Flows of Sintered NdFeB Magnets and Li-Ion Batteries Reported vs. Embedded US Imports, *Miner. Econ.*, 2023 <https://doi.org/10.1007/s13563-023-0038-1-3>
13. M. Zakotnik, I.R. Harris, and A.J. Williams, Multiple Recycling of NdFeB-Type Sintered Magnets, *J. Alloy Compd.*, 2009, **469**, p 314–321
14. L. Weiqiang, L. Chao, Z. Miha, Y. Ming, Z. Dongtao, and H. Xiulian, Recycling of Waste Nd-Fe-B Sintered Magnets by Doping with Dysprosium Hydride Nanoparticles, *J. Rare Earhts*, 2015, **33**, p 846–849
15. N. Chuewangkam, S. Pinitsoontorn, and P. Chindaprasirt, Properties of NdFeB Magnetic Cement, *J. Cem. Concrete Compos.*, 2019, **103**, p 204–212
16. G. Alecu and W. Kappel, Element of Circular Economy in the Manufacture of NdFeB Permanent Magnets IN ICPE-CA, *J. Eng. Sci. Innov.*, 2021, **6**(2), p 175–188
17. K. Zhang, E. Fan, J. He, X. Li, and Y. Huang, Long-Term Effects of Electrochemical Corrosion on Magnetic Properties of Sintered NdFeB Magnets, *J. Magn. Magn. Mat.*, 2021, **538**, p 168309
18. Y. Wu, M. Zhu, Q. Sun, L. Zhang, P. Shen, and Y. Fang, Superior Corrosion Resistance and Corrosion Mechanism of Dual-Phase (Ce₁₅Nd₈₅)₃₀Fe_{bal}B₁M Magnets in Different Solutions, *J. Rare. Earths*, 2023, **41**, p 122–129
19. E. Emil-Kaya, B. Polat, S. Stopic, S. Gürmen, and B. Friedrich, Recycling of NdFeB Magnets Employing Oxidation, Selective Leaching, And Iron Precipitation in an Autoclave, *Rsc Adv.*, 2023, **13**, p 1320–1332
20. L. Yang, J. Ouyang, Z.M. Wang, and G.L. Song, The early-Stage Propagation of Localized Corrosion of a Sintered NdFeB Alloy in Aqueous Environments, *J. Mater. Eng. Perform.*, 2023 <https://doi.org/10.1007/s11665-023-08280-y>
21. X. Li, J. Ni, Z. Wang, B. Song, C. Wang, and X. Cui, Effects of Pressure Holding Time on Magnetic Properties and Corrosion Resistance of Hot-Deformed NdFeB Magnets, *J. Mater. Eng. Perform.*, 2023 <https://doi.org/10.1007/s11665-023-08575-0>
22. L. Li, X.T. Wei, Z.Y. Li, and X. Cheng, Corrosion resistance analysis of sintered NdFeB magnets using ultrasonic-acided EDM method, *J. Mater. Eng. Perform.*, 2015, **24**, p 536–542
23. Z. Liu, J. He, Q. Zhou, Y. Huang, and Q. Jiang, Development of Non-rare Earth Grain Boundary Modification Techniques for Nd-Fe-B Permanent Magnets, *J. Mater. Sci. Tech.*, 2022, **98**, p 51–61
24. Q. Zhou, W. Li, Y. Hong, L. Zhao, X. Zhong, H. Yu, L. Huang, and Z. Liu, Microstructure Improvement Related Coercivity Enhancement for Sintered NdFeB Magnets after Optimized Additional Heat Treatment, *J. Rare Earths*, 2018, **36**(4), p 379–384
25. S. Humaidi, Achiruddin, K. Sembiring, Hanifah, N. Rusnaeni, and Muljadi, Nd-Rich Effects on Structural and Magnetic Properties of Nd₂Fe₁₄B Magnets, *J. Mech. Indus. Eng.*, 2017, **2**, p 189–193
26. T. Song, H. Wang, X. Tang, W. Yin, Z. Wang, J. Ju, R. Chen, and A. Yan, The Effects of Nd-Rich Phase Distribution on Deformation Ability of Hydrogenation-Disproportionation-Desorption-Recombination Powders and Magnetic Properties of the Final Die-Upset Nd-Fe-B Magnets, *J. Magn. Magn. Mater.*, 2019, **476**, p 194–198
27. J. Huang, Q. Liu, Z. Yang, G. Xu, P. Zhang, J. Lv, W. Sun, B. Li, D. Wang, and Y. Wu, Densification and Anticorrosion Performances of

- Vacuum Evaporated Aluminium Coatings on NdFeB Magnets, *J. Rare Earths*, 2021, **39**(10), p 1238–1245
28. X. Su, L. Zhu, W. Li, H. Chen, R. Cao, and H. Liu, Effect of Alumina Sol on Formation and Properties of Electrodeposited Zinc Coatings on NdFeB Magnet, *Surf. Interfaces*, 2020, **21**, p 100776
 29. Y. Yang, N. Jiang, Y. Sun, L. Yang, C. Guan, E. Zhang, X. Fang, and J. Liu, Structure and Corrosion Resistance Characteristics of ZnAl/EP Coating on Bonded NdFeB Magnet, *J. Mater. Eng. Perform.*, 2023, **32**, p 5475–5482
 30. Y. Yang, Y. Wang, L. Yang, R. Ren, Y. Chen, B. Dong, J. Liu, X. Fang, and Q. Gao, The Preparation and Properties of ZnAl Coating for Ring-Shaped Bonded NdFeB Magnet with High Corrosion Resistance, *J. Mater. Eng. Perform.*, 2022, **31**, p 1003–1008
 31. W. Chen, Y.L. Huang, J.M. Luo, Y.H. Hou, X.J. Ge, Y.W. Guan, Z.W. Liu, Z.C. Zhong, and G.P. Wang, Microstructure and Improved Properties of Sintered Nd-Fe-B Magnets by Grain Boundary Diffusion of Non-Rare Earth, *J. Magn. Magn. Mater.*, 2019, **476**, p 134–141
 32. J. Tao, B. Liu, P. Zhang, G. Xu, J. Lv, J. Huang, J. Yan, W. Sun, B. Li, D. Wang, and Y. Wu, Anti-Corrosion Performance of Si-Surface-Alloying NdFeB Magnets Obtained with Magnetron Sputtering and Thermal Diffusion, *J. Rare Earths*, 2023, **41**(8), p 1203–1210
 33. M.F. Kılıçaslan, B. Akgül, and Y. Yılmaz, Evolution of the Magnetic Properties of Melt-Spun NdFeB Alloys with the Addition of Waste NdFeB Magnet, *J. Mater. Sci. Mater. Electron.*, 2023, **34**, p 1230
 34. H. Chen, X. Yang, L. Sun, P. Yu, X. Zhang, and L. Luo, Effects of Ag on the Magnetic and Mechanical Properties of Sintered NdFeB Permanent Magnets, *J. Magn. Magn. Mater.*, 2019, **485**, p 49–53
 35. Q. Zhou, R. Tang, F. Xiao, and Z. Liu, Coercivity Enhancement of Nd–Ce–Fe–B Sintered Magnets by the Grain Boundary Diffusion Process Using Nd–Al–Cu Alloy, *IEEE Trans. Magn.*, 2018, **54**(11), p 2102804
 36. H.X. Zeng, Q.X. Wang, J.S. Zhang, X.F. Liao, X.C. Zhong, H.Y. Yu, and Z.W. Liu, Grain Boundary Diffusion Treatment of Sintered NdFeB Magnets by Low Cost La-Al-Cu Alloys With Various Al/Cu Ratios, *J. Magn. Magn. Mater.*, 2019, **490**, p 165498
 37. S. Hu, J. Liu, Y. Liu, J. Zhang, H. Yu, K. Su, Y. Huang, and Z. Liu, Enhancing the Properties of Spark Plasma Sintered Nanocrystalline NdFeB Magnets by the Addition of Cu-Zn Alloy and Dy₂O₃ Powders, *J. Electron. Mater.*, 2020, **49**, p 720–727
 38. K. Lu, X. Bao, Y. Zhou, X. Lv, Y. Ding, M. Zhang, C. Wang, and X. Gao, Effect of Al/Cu on the Magnetic Properties and Microstructure of Nd-Fe-B Sintered Magnet by Diffusing Pr-Tb-(Cu, Al) Alloys, *J. Magn. Magn. Mater.*, 2020, **500**, p 166384
 39. L. Zhao, J. He, W. Li, X. Liu, J. Zhang, L. Wen, Z. Zhang, J. Hu, J. Zhang, X. Liao, K. Xu, W. Fan, W. Song, H. Yu, X. Zhong, Z. Liu, and X. Zhang, Understanding the Role of Element Grain Boundary Diffusion Mechanism in Nd–Fe–B Magnets, *Adv. Funct. Mater.*, 2022, **32**(8), p 2109529
 40. W. Song, J. He, Z. Yu, J. Cao, X. Liao, W. Fan, H. Yu, H. Mao, C. Mao, and Z. Liu, Enhancing the Grain Boundary Diffusion Efficiency of Tb for Nd-Fe-B Magnets Using Dual-Alloy Diffusion Source, *J. Mater. Res. Technol.*, 2022, **18**, p 841–851
 41. M. Pan, P. Zhang, Q. Wu, and H. Ge, Improvement of Corrosion Resistance and Magnetic Properties of NdFeB Sintered Magnets With Cu and Zr Co-Added, *Int. J. Electrochem. Sci.*, 2016, **11**(4), p 2659–2665
 42. W. Liu, C. Li, M. Zakotnik, M. Yue, D. Zhang, and X. Huang, Recycling of Waste Nd-Fe-B Sintered Magnets by Doping with Dysprosium Hydride Nanoparticles, *J. Rare Earths*, 2015, **33**(8), p 846–849
 43. M. Zakotnik and C.O. Tudor, Commercial-Scale Recycling of NdFeB-Type Magnets with Grain Boundary Modification Yields Products with ‘Designer Properties’ that Exceed those Of Starting Materials, *Waste Manag.*, 2015, **44**, p 48–54
 44. D. Givord, P. Tenaud, and J.M. Moreau, Refinement of the Crystal Structure of R_{1+x}Fe₄B₄ Compounds (R = Nd, Gd), *J. Less-Common Met.*, 1986, **123**(1–2), p 109–116
 45. Q. Zhou and S. Liu, Fabrication of Magnesium Phosphate Coating by Electrochemical Cathodic Method for Corrosion Protection of Sintered NdFeB Magnets, *J. Mater. Eng. Perform.*, 2021, **30**(2), p 1200–1206

Publisher's Note Springer Nature remains neutral with regard to jurisdictional claims in published maps and institutional affiliations.

Springer Nature or its licensor (e.g. a society or other partner) holds exclusive rights to this article under a publishing agreement with the author(s) or other rightsholder(s); author self-archiving of the accepted manuscript version of this article is solely governed by the terms of such publishing agreement and applicable law.